Title

Seismic behavior of shallow buried water reservoirs via large scale three-dimensional numerical models

Authors

AlKhatib, Karim
Hashash, Youssef MA
Ziotopoulou, Katerina

Publication Date

2024-12-01

DOI

10.1016/j.soildyn.2024.109005

Peer reviewed

Soil Dynamics and Earthquake Engineering 187 (2024) 109005

Contents lists available at ScienceDirect

Soil Dynamics and Earthquake Engineering

journal homepage: www.elsevier.com/locate/soildyn

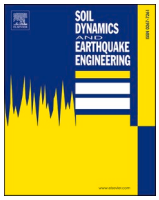

Seismic behavior of shallow buried water reservoirs via large scale three-dimensional numerical models

Karim AlKhatib [a,*], Youssef MA. Hashash [b], Katerina Ziotopoulou [c]

[a] Mott MacDonald, Cleveland, OH, 44135, USA
[b] Department of Civil and Environmental Engineering, University of Illinois Urbana-Champaign, Urbana, IL, 61801, USA
[c] Department of Civil and Environmental Engineering, University of California, Davis, CA, 95616, USA

ARTICLE INFO

Keywords:
Buried water reservoirs
Fluid-structure-soil interaction
Nonlinear finite element
Seismic analysis
Progressive collapse
Parametric study

ABSTRACT

As buried water reservoirs are increasingly being utilized to store and deliver water, they are now regarded as critical infrastructures that must continue to operate in the event of an earthquake. This paper presents the results of a large-scale numerical parametric study that was carried out to advance our understanding of the seismic fluid-structure-soil interaction (FSSI) response of buried water reservoirs. Advanced nonlinear three-dimensional (3D) FSSI numerical models of reservoirs were employed while considering reservoir size, embedment depth, soil profile, and ground motion variability. The study showed that, unlike other conventional underground structures, the peak ground acceleration (PGA) has the strongest correlation to the reservoir seismic response. Increasing the embedment depth or reservoir size was found to generally increase the demands on the structural elements while reducing the base and backfill slippage. Softer sites were found to cause an increase in the roof racking and including the vertical component of the motion increased the water dynamic pressures. Among the columns, the ones closest to the center were found to experience the highest demands and the ones at the corner the lowest. In fact, in some extreme cases, a total collapse of the reservoir was initiated by column failure due to the lack of structural redundancy. The roof in-plane shear stresses were observed to accumulate near the walls, indicating a diaphragm behavior. The reservoir's unique seismic response compared to other underground structures makes generalizing the commonly used simplified design procedures inapplicable. Instead, 3D FSSI numerical models were demonstrated to be a reliable tool for the seismic design of buried reservoirs.

1. Introduction

The necessity for water storage coupled with the demand for high water quality have made underground reservoirs an appealing solution for urban areas. Their compact footprint and ability to protect water from external elements make them an attractive choice. However, despite their increasing adoption, the seismic behavior of buried reservoirs is not well understood. As a result, the currently employed design procedures for seismic design of reservoirs mostly rely on those used for conventional underground structures [1,2], raising uncertainty about their applicability.

The seismic response of most underground structures is predominantly controlled by the kinematic interaction with the surrounding soil [1]. This has led to the development of design methods that explicitly consider seismic ground deformation, such as the Seismic Deformation Method [3]. For linear underground structures, like tunnels and subway stations, deformation evaluations in the transverse and longitudinal planes are typically decoupled and analyzed under the plane strain assumption. This common understanding has resulted in the erroneous extension of these assumptions and approaches to the seismic design of reservoirs, merely because they share the common characteristic of being constructed underground. However, applying these assumptions and approaches to reservoirs can be problematic due to two critical differences: (i) reservoirs are typically buried at shallow depths, and they exhibit unique aspect ratios and structural configurations [4] that differ from other underground structures, and (ii) the presence of stored water produces additional seismic demands due to its sloshing and slamming against the reservoir's structural components during earthquakes.

Buried reservoirs are a relatively new class of structures and as such,

* Corresponding author.
E-mail address: karim.alkhatib@mottmac.com (K. AlKhatib).

https://doi.org/10.1016/j.soildyn.2024.109005
Received 22 May 2024; Received in revised form 26 August 2024; Accepted 29 September 2024

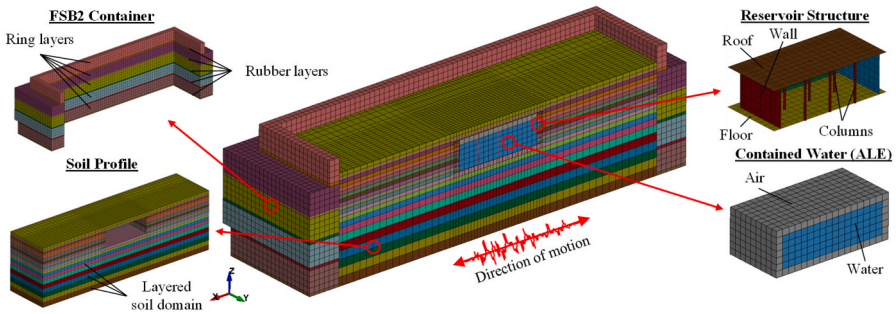

Fig. 1. 3D FE model used in AlKhatib et al. [14] to replicate the FSSI centrifuge experiments in the validation phase only.

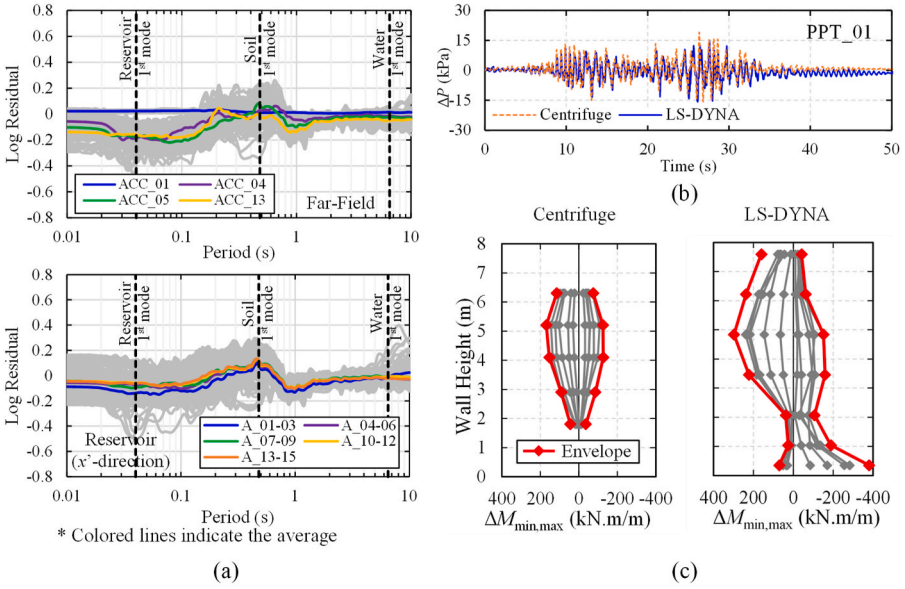

Fig. 2. Example results of the centrifuge FE model validation [14]: (a) log residual of the computed 5 % damped spectral acceleration of soil and reservoir, (b) stored water dynamic pressure time-history, and (c) wall dynamic bending moment.

in-depth research on their seismic behavior is lacking. However, a case history of buried reservoir failure was documented following the M_w 6.6 San Fernando Valley Earthquake in 1971 [5]. More recently, four newly constructed reservoirs in Seattle, Washington were identified to be seismically deficient which required implementing costly structural retrofits [6]. These, as well as other case histories, highlight the need to fundamentally address the shortcomings in seismic design practice and enhance the seismic resilience of these critical structures.

Few studies have explored the seismic response of reservoirs through experimental or numerical modeling. Hushmand et al. [7,8] conducted centrifuge model tests to investigate the seismic structure-soil-interaction (SSI) response of 2D simplified representations of buried reservoirs. They concluded that existing simplified procedures failed to accurately capture the magnitude and distribution of seismic earth pressures experienced by reservoirs. Some numerical studies have focused on the seismic performance of buried reservoirs many of which considered a 2D representation [9–12]. Notably, in the seismic evaluation program for the Seattle reservoirs [6], both two- and three-dimensional models were employed to provide a more detailed evaluation.

This paper presents a large-scale numerical parametric study aimed at studying the seismic fluid-structure-soil interaction (FSSI) response of buried water reservoirs. Advanced nonlinear three-dimensional (3D) FSSI numerical models of reservoirs were developed using LS-DYNA [13], a finite element (FE) package. The numerical modelling approach was validated in previous study by the authors to yield reliable results when compared to centrifuge model test recordings [14]. The numerical models employed in this parametric study alleviate the centrifuge test limitations by adopting a more realistic representation of the problem. Nonlinear material models were employed for both the structure and the soil, while the stored water was explicitly modeled using the Arbitrary Lagrangian Eulerian (ALE) formulation. The contacts between the different domains of the model were established using coupling algorithms with contact parameters calibrated against centrifuge experimental results. The study investigated various key parameters that affect seismic behavior, including reservoir size, embedment depth, soil profile, and ground motion variability, yielding a total of 840 different cases/simulations.

The study showed that amongst the input motion's peak response parameters, peak ground acceleration (PGA) has the strongest correlation to the seismic response of the reservoir. This observation suggests that the seismic demand on the structure is mainly driven by the reservoir's inertia, such as the mass of the roof, rather than the kinematic interaction between the reservoir and the surrounding soil, which is commonly observed in other conventional underground structures. The increase in the embedment depth or the reservoir size was found to generally increase demands on structural elements while decreasing base slippage. Softer soil conditions resulted in increased roof racking, and considering the vertical component of the input motion increased water dynamic pressures. Columns closest to the center of the reservoir experienced the highest demands, sometimes leading to total reservoir collapse due to the lack of structural redundancy. The roof was observed

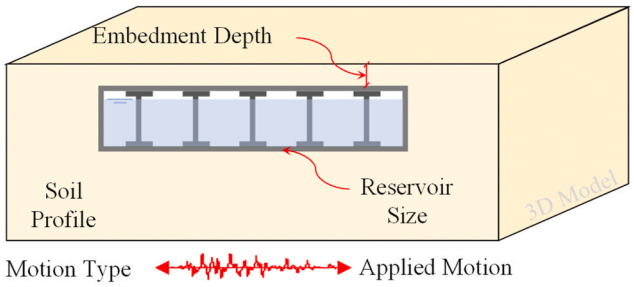

Example Model Name:

R01 S01 D01 2D M01

Reservoir Size	Soil Profile	Embedment Depth	Motion Type	Applied Motion
R01; R02	S01; S02; S03	D01; D02	2D; 3D	M01 to M35

Fig. 3. Parameters included in the parametric study and FE model naming convention.

to function as a diaphragm system, distributing seismic demands to the vertical lateral resisting elements, particularly the walls. This was observed through the gradual increase of in-plane shear stresses from the center towards the resisting walls. Finally, the reservoir behavior was evaluated to be inherently 3D and quite complex compared to other typical underground structures, thus emphasizing the necessity of analyzing it using high fidelity 3D FSSI numerical models.

2. Reservoir's centrifuge experiments, model validation and limitations

As part of a broader research project, two series of centrifuge model tests were carried out using the large 9 m-radius centrifuge at the Center for Geotechnical Modeling (CGM) at the University of California, Davis. The first series, conducted by Morales [15], investigated the hydrodynamic forces exerted on the interior of a rigid tank structure. This involved subjecting a rectangular structure of variable lengths and filled at a range of water depths to a multitude of input motions within a hypergravity environment [16,17]. Subsequently, AlKhatib et al. [17] developed ALE models to reproduce the centrifuge experiments of Morales [15] in addition to other 1g shake table experiments available in the literature. The results of the numerical simulations, simplified approaches, and analytical methods were compared to the experimental recordings, in terms of free surface elevation and hydrodynamic pressures, to evaluate the applicability and inherent limitations of each methodology. Among other findings, the study showed the reliability of numerical models in capturing water dynamic responses, demonstrating their broad applicability for use in complex problems of FSSI.

The second model test series [14,18] was performed to expand the understanding of system-level performance and investigate the complete FSSI problem in conditions more akin to real-world field scenarios. The model reservoir structure, constructed from fabricated aluminum metal using a bolted construction design, was buried at a shallow depth within a dry deposit of medium-dense sand. The experimental program consisted of two sets, differing in the reservoir orientation relative to the direction of shaking to include pseudo 2D motion effects. Both sets subjected the buried reservoir structure to a series of broadband earthquake motions at the bottom of the Flexible Shear Beam (FSB2) centrifuge container and included different levels of water filling. These levels progressed from an initially empty reservoir to a "full" condition, mimicking typical freeboard conditions. In parallel, AlKhatib et al. [14] developed corresponding numerical models, as shown in Fig. 1, wherein the structure and soil domains were represented by continuum Lagrangian FE, while the fluid was modeled with the validated ALE formulation. The simulations successfully captured the experimentally recorded reservoir responses in terms of soil and reservoir accelerations, bending moment increments, and dynamic water pressures, as shown in Fig. 2. The study demonstrated that the complex seismic response of buried reservoirs is best captured by conducting a 3D FSSI numerical simulation. Nevertheless, the models represented in the centrifuge experiments and the corresponding numerical simulations had some important limitations.

- *Reservoir size constraints:* Reservoirs are characterized by their huge scale compared to other underground structures, as shown in Table 1. The need to balance a reasonably sized model structure, a realistic depth of the soil deposit, and fit those in FSB2 centrifuge container led to compromises in the size of the model structure that could be fit in the available lateral dimensions of the FSB2 container. Therefore, the reservoir size was relatively small, compared to a typical case, which resulted in a stiffer structure. It was only possible to place a total of 9 columns inside the reservoir model to maintain a typical column spacing of 6 m. Furthermore, unlike the aluminum reservoir centrifuge model structure, reservoirs are constructed using reinforced concrete, and the wall, roof, and slab are not necessarily of the same thickness.
- *Soil profile representation:* Experimental methods are not intended to nor can they replicate the exact conditions found in real-world soil profiles. This is due to the non-homogeneity and anisotropy of soil profiles, which may be found in both natural deposits and man-made earth fills. The soil profile realized in the experiments consisted of uniform medium-dense Ottawa sand. The depth of the profile was limited to the total depth of the FSB2 container minus a freeboard distance. In real sites, however, the stratigraphy is composed of multiple layers with different properties and can reach deeper depths before reaching the top of rock. The presence of a multilayer profile would affect the amplification/attenuation of the seismic waves as they travel from the bedrock to the surface. Moreover, as the seismic waves travel from one layer to another, reflection and refraction occur depending on the angle of incidence and impedance ratio at the layer-to-layer interface which were overlooked by having uniform soil profiles.
- *Influence of centrifuge container:* The seismic soil reaction might be altered by the centrifuge container representing the model's lateral boundary condition. The type and size of the container can have an impact on the seismic soil response of vertically propagating shear waves. In centrifuge experiments, this effect can be reduced by utilizing a flexible shear beam container such as the FSB2 container. Nonetheless, its natural frequency is typically lower than the original natural frequency of the soil [19] and, depending on the soil's stiffness response, its effects may be accentuated (e.g., Ref. [20]). In addition, the container bottom, which is the source of input motion to the soil, represents an artificial and rigid geologic transition. Therefore, in the centrifuge FE models of AlKhatib et al. [14], the container was explicitly modeled to accurately represent the experimental conditions and include the container effects.
- *Input motion:* The input motions applied at the base of the centrifuge container were scaled and filtered to avoid resonance with the container's first fundamental period. In the rotated reservoir configuration (BRE-R), the ground motion was applied at 30° from the reservoir's principal x'-axis [14] in an attempt to include 2D effects. However, that only imposed a "pseudo" 2D motion effects on the reservoir since, in real 2D motions, the two horizontal components are not a scale of one another.

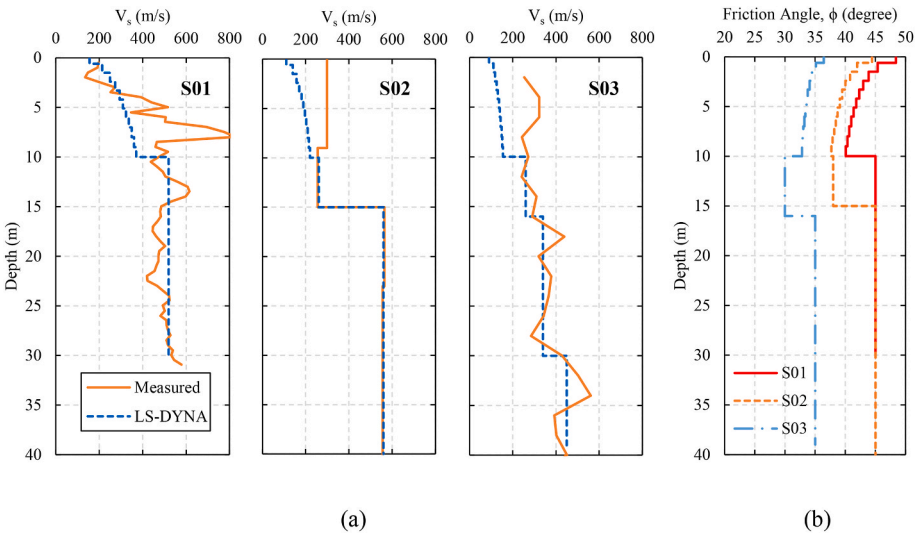

Fig. 4. Profiles of (a) shear wave velocities and (b) friction angle of S01, S02, and S03.

In this parametric study, the validated numerical modelling technique [14] was used while alleviating the aforementioned centrifuge test limitations through adoption of a more realistic representation of the problem. This enabled the investigation of key parameters affecting the reservoir seismic response while using a high-fidelity numerical model.

3. Parametric study design

The study investigated the effect of key parameters affecting the reservoir FSSI behavior which included: (1) reservoir size, (2) soil profile, (3) embedment depth, (4) motion intensity, and (5) motion type (2D vs. 3D). The number of cases for each parameter is summarized in Fig. 3, yielding a total of 840 distinct cases/simulations.

(1) *Reservoir size*: Two different sizes of reservoirs were investigated representing a small, R01, and a medium, R02, reservoir. Both reservoirs had similar height, column spacing, and cross-sectional characteristics, but differ in their footprint area. Table 2 lists the dimensions and sectional properties of both reservoirs. The selection of these dimensions was guided by real-world examples listed in Table 1.

(2) *Site class*: Soil layers in the field are often of different conditions and properties which affect the seismic response of buried reservoirs. Three profiles (S01, S02, and S03) were utilized in the parametric study, representative of different site classes as per ASCE/SEI 7–22 [21] based on their time-averaged shear wave velocities of the upper 30 m of soil profile (V_{s30}), as shown in Table 3. Leveled sites with no topographical features were considered. All three soil profiles were collected from real sites located on the US west coast. The site classes ranged from Site Class C to DE. The native profiles were altered to include 10 m of fill at the top of the profile to reflect the construction sequence of these structures. The relative density (D_R) of the fill ranged from medium dense, for the softest site (S03), to very dense fill, for the stiffest site (S01). The original and used shear wave velocity profiles for all sites are shown in Fig. 4(a). The friction angle (ϕ) for each layer, shown in Fig. 4(b), were obtained using Bolton [22], correlated friction angles from corrected standard penetration test blow counts, if available, or typical values. Reservoirs are typically situated at high elevations and are buried at relatively shallow depths to leverage gravity for water delivery. This result in the water table being found way below the bottom of the reservoir for most cases [6]. Therefore, it was decided to use dry profiles with no water table for the purpose of this study.

(3) *Embedment depth*: Reservoirs are typically located at shallow depths with a relatively thin layer of backfill (e.g., 0.5–2 m). The embedment depth, defined as the distance between the ground surface and the top of the roof, impacts the initial static condition such as the bending moment in the roof and the axial load in the columns. Therefore, increasing the embedment depth would increase the overburden pressure imposed on the reservoir as well as impacting the dynamic earth pressures during earthquakes. Furthermore, the mass of the overlaying backfill also contributes to the available overall inertial mass of the roof. This implies that the embedment depth is an important parameter to be considered in the parametric study. Therefore, two embedment depths were examined: 0.6 and 1.5 m denoted hereafter as D01 and D02, respectively.

(4) *Selection of ground motions*: During seismic design, ground motion records are typically selected and scaled to match the specific seismic source characteristics and hazard levels of a given site. For this study, however, a suite of real ground motions was selected to simulate the seismic response of the reservoirs and to capture uncertainty and variability by covering a wide range of source and input motion characteristics. This approach ensures that the reservoir experiences various intensities of real ground motions, thereby avoiding any bias in the results and conclusions drawn. Thirty-five (35) ground motions (denoted as M01 to M35) were selected with different source mechanisms, amplitudes, and time durations. The motion records were obtained from online resources such as the PEER and KiK-net/K-NET ground motion databases. No modification, scaling, or filtering was applied to the motion components. However, to prevent any permanent displacement at the base, some motions (e.g., KiK-net/K-NET motions) needed to be baseline corrected. The distribution of seismic source characteristics and spectral plots of the input ground motions are shown in Fig. 5.

(5) *Impact of vertical motion*: A seismic ground motion can be decomposed into three components: two horizontal and one vertical. The findings of AlKhatib et al. [14] demonstrated that, compared to 1D motions, 2D motions increase the demands on the reservoir especially at the corners. In this parametric study, the inclusion of the third (vertical) component in the simulation was investigated. Often enough, designers in practice ignore the vertical component or even consider one-dimensional motion in their simulations. This may underestimate some of the demands imposed by the vertically oriented motion component. Therefore, all the simulations were subjected to the 35 ground motions in

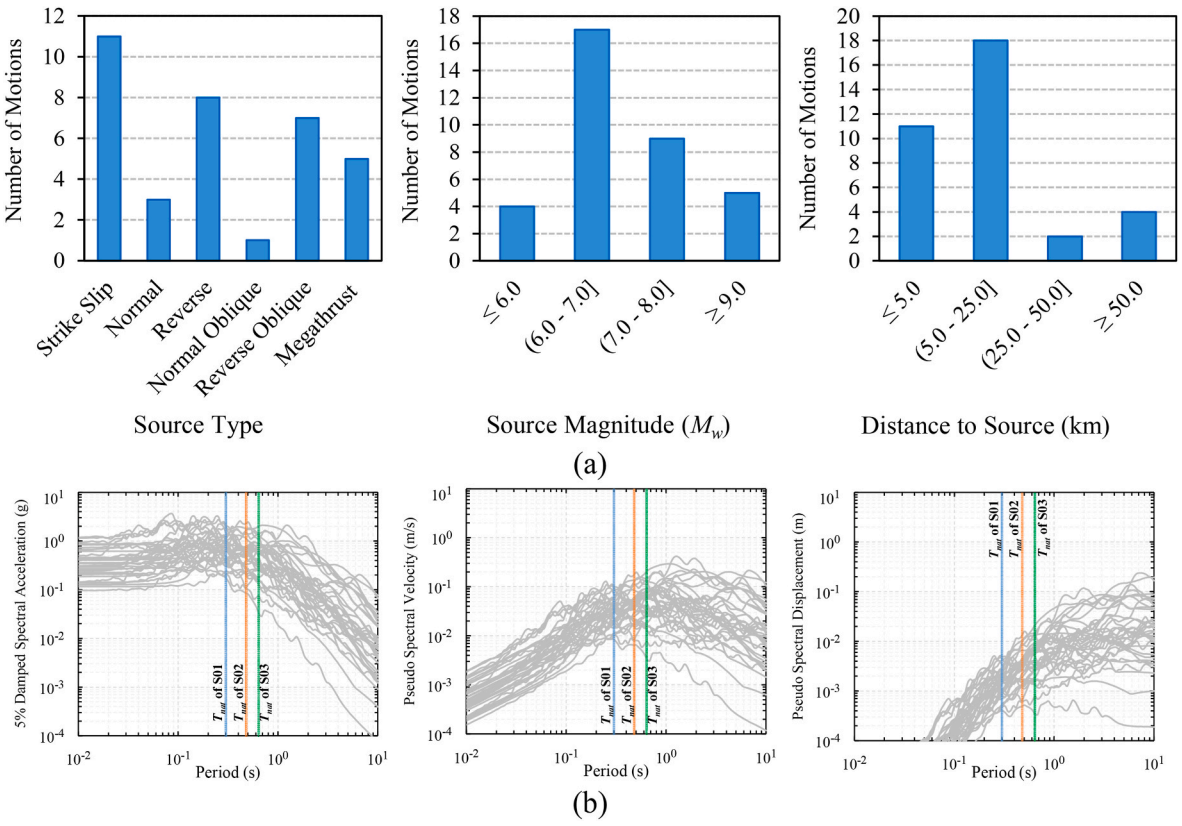

Fig. 5. Summary of the ground motion (a) source characteristics and (b) spectral plots while superimposing the three selected sites' natural periods.

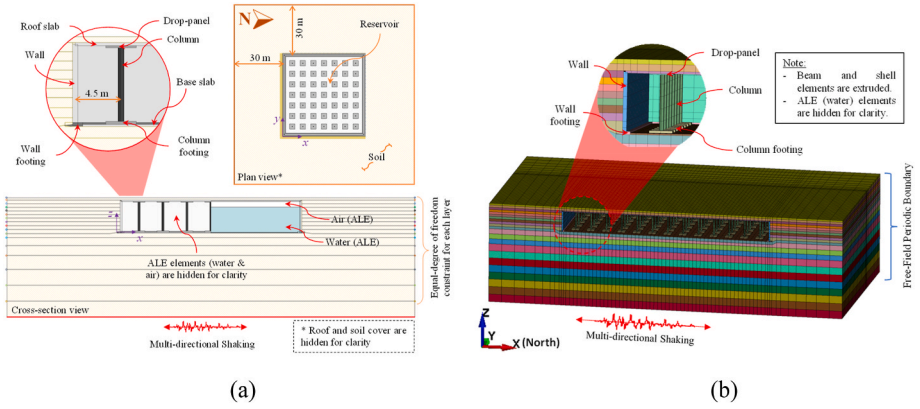

Fig. 6. The 3D FSSI FE model used in this study: (a) elements and dimensions (showing the case of R01_D01_S01), and (b) 3D rendering of the model (showing the case of R02_D02_S03).

two different scenarios: (1) taking into account the two horizontal components only (denoted as 2D), and (2) taking into account all three components of the motions (denoted as 3D).

4. Finite element model description

Modeling techniques and parameters used in the calibrated and validated centrifuge FE models of AlKhatib et al. [14], especially contact parameters, were utilized in this study. Nevertheless, the parametric study simulations considered a more accurate representation of the reservoir structural material and configuration, as well as soil layering and boundary conditions. The naming convention followed for the 840 cases/simulations is shown in Fig. 3. A view of the 3D FSSI FE model used in this parametric study is shown in Fig. 6. Table 4 lists general statistics of the model contents and simulation time.

4.1. Multilayer soil profile

The multilayered soil profile, presented in Table 3, was numerically modeled using eight-node constant stress solid elements with hourglass control and was divided into sublayers to allow for maximum shear wave frequency propagation of at least 30 Hz. Pressure-dependent shear modulus reduction and damping curves for each soil layer were generated following the formulation proposed by Darendeli [23] and then corrected to reach 95 % of the shear strength at 10 % shear strain according to the General Quadratic/Hyperbolic model proposed by Groholski et al. [24]. I-soil constitutive model, developed by Numanoglu et al. [25] and implemented in LS-DYNA as a user-defined material

Table 1
Examples of existing buried water reservoirs located in the western US.

Reservoir	Location	Capacity (ML)	Footprint (m × m)	Wall		Slab Thk		Columns		Other details
				Hgt (m)	Thk (cm)	Roof (cm)	Base (cm)	Spacing (m)	Ø (cm)	
Myrtle[a]	Seattle, WA	19	53 × 47	7.6	56	28	15	6.1	61	0.6-m backfill cover
Walteria[b]	Torrance, CA	38	54 × 103	4.3	30	24	15	6.1	41 × 41	0.6-m backfill cover
5B[b]	Pomona, CA	38	57 × 121	5.5	30	15	15	6.4	46 × 76	Half buried
West Seattle[a]	Seattle, WA	121	138 × 138	6.7	43	28	15	6.1	61	0.6-m backfill cover
Balboa[c]	Granada Hills, CA	189	152 × 158	5.4	53	36	41	6.1	61	2.4-m backfill cover
Beacon[a]	Seattle, WA	189	165 × 152	6.7	53	28	15	6.1	61	0.6-m backfill cover
Maple Leaf[a]	Seattle, WA	227	203 × 151	7.3	56	28	15	6.1	61	0.6-m backfill cover; 56-cm divider wall
Dunsmuir[b]	Oakland, CA	244	171 × 122	9.8	56	22	30	5.8	61	0.6-m backfill cover
Headworks[d]	Los Angeles, CA	416	317 × 200	10.7	122	51	91	9.1	91	0.6-m backfill cover; divided into 2 cells

Note: values are not exact.
[a] CH2MHILL [6].
[b] Kenmir [4].
[c] Jennings [5].
[d] Hudson et al. [10].

Table 2
Reservoir structural configurations used in the parametric study.

Reservoir I.D.	Dimensions (m)			Columns Spacing (m)	Section Thickness in cm (Reinforcement Percentage)				Stored water 1st and 2nd mode periods (s)
	L	W	H		Walls[a]	Slab	Roof	Columns	
R01	47	47	8.0	6.0	50 (1.6/0.7)	20 (0.5)	30 (0.8)	Ø = 60 (1.4)	11.7 4.70
R02	83	83	8.0	6.0	50 (1.6/0.7)	20 (0.5)	30 (0.8)	Ø = 60 (1.4)	20.7 7.40

[a] Reinforcement percentage in vertical (v) and horizontal (h) directions are reported as (v/h).

Table 3
Soil profiles used in the parametric study.

Profile I.D.	Reference Profile		Site Class (ASCE7-22)	Depth (m)	V_{s30} (m/sec)	T_{nat} (s)
	Source	Location				
S01	[6]	Seattle, WA	CD	30	408	0.3
S02	[26]	Granada Hills, CA	D	40	294	0.48
S03	[26]	Oakland, CA	DE	39	213	0.64

Note: T_{nat} is the fundamental period of the soil profile.

Table 4
The 3D FSSI FE model statistics.

Model Component	Total Number[a]
Soil brick elements	33,284–95,384
Reservoir shell elements	2,948–7,844
Reservoir beam elements	245–845
ALE brick elements	6,144–18,816
Nodes	50,374–140,876
Intel Xeon E5-2683 @ 2.1 GHz and 128 GB of available RAM (Windows Server)	
Timestep	1.95×10^{-4} s
Runtime[a] (on 4 cores)	0.2–0.6 h/1 s of motion

[a] Depends on the soil profile and reservoir size being simulated.

model for soil, was used. The framework of I-soil is composed of multiple layers of slider-spring pairs. The spring represents the stiffness, while the slider represents the shear strength of each layer. Connected in series, the spring and slider exhibit elastic-perfectly plastic behavior. These

Table 5
Input parameters for the soil material model.

Parameter	Value
Darendeli [23]	
At-rest lateral earth pressure coefficient, K_o	0.4
Plasticity index, PI	0
Over-consolidation ratio, OCR	1
Loading frequency	1
Number of loading cycles	10
I-soil [25]	
Density, ρ (kg/m^3)	1735
Poisson's ratio, υ	0.3
Cut-off Pressure, P_o (kPa)	−1
Stiffness PD coefficient, b	0.5
Strength PD parameters a_0, a_1, a_2	0, 0, 1
Volumetric strains parameters η_{dsr}, A_0	0.51, 0.4

pairs, with different parameters, are nested in parallel, collectively producing a nonlinear shear stress-strain curve. In this study, 30 layers were used to form the backbone of the full stress-strain behavior of the soil, as recommended by Numanoglu et al. [25]. The strength and stiffness pressure-dependency along with the shear-induced volumetric response were employed in the material model while using recommended values for the corresponding parameters as shown in Table 5. Frequency independent viscous damping, with frequencies ranging from 0.1 to 30 Hz, was used to represent soil damping at small strains, in lieu of frequency dependent Rayleigh damping formulation. The range of frequency was chosen such that it covers the frequencies imposed by the base motion while keeping a ratio of $F_{high}/F_{low} \leq 300$, as suggested by

Table 6
Input parameters for reinforced concrete material model (MAT-172).

Parameter	Value
Density, ρ (kg/m^3)	2400
Concrete	
Young's Modulus, E (GPa)	24.8
Poisson's Ratio, ν	0.2
Compressive strength, f_c' (MPa)	28
Tension strength, f_t' (MPa)	2.8
Steel Reinforcement	
Young's Modulus, E (GPa)	200
Poisson's Ratio, ν	0.3
Yield strength, f_y (MPa)	420

the LS-DYNA manual [13]. The small-strain damping ratio for each soil layer was obtained from the Darendeli [23] formulation (e.g., D_{min}).

To minimize boundary effects, the soil domain was extended 30 m beyond the reservoir walls, a distance found sufficient by CH2MHILL [6]. A free-field periodic boundary was implemented at the nodes on the four vertical sides of the soil domain to prevent side reflections. This was accomplished by constraining soil nodes at the same depth to deform identically in all three directions, thereby simulating an infinite free-field medium. The input ground motion was applied to the rigid base of the model. In the case of 2D motion, bidirectional acceleration was applied at the bottom soil nodes in the x and y directions, with constraints preventing movement in the z direction. In the case of 3D motion, the bottom nodes were assigned a prescribed 3D acceleration in all three directions without restraints. The contact between soil and reservoir was established using a surface-to-surface contact algorithm that solves for both normal and frictional forces. The constant soil-reservoir friction coefficient of 0.51 (e.g., $^2/_3 \tan 37°$) was considered for all models.

Table 7
Water material properties and related Grüneisen EOS parameters.

	Material Properties		Grüneisen EOS parameters					
Material Parameter	Density (kg/m^3)	Dynamic Viscosity (Pa.s)	C (m/s)	S_1	S_2	S_3	γ_0	a
Value used	1000	8.9×10^{-04}	1647	1.921	−0.096	0	0.35	0

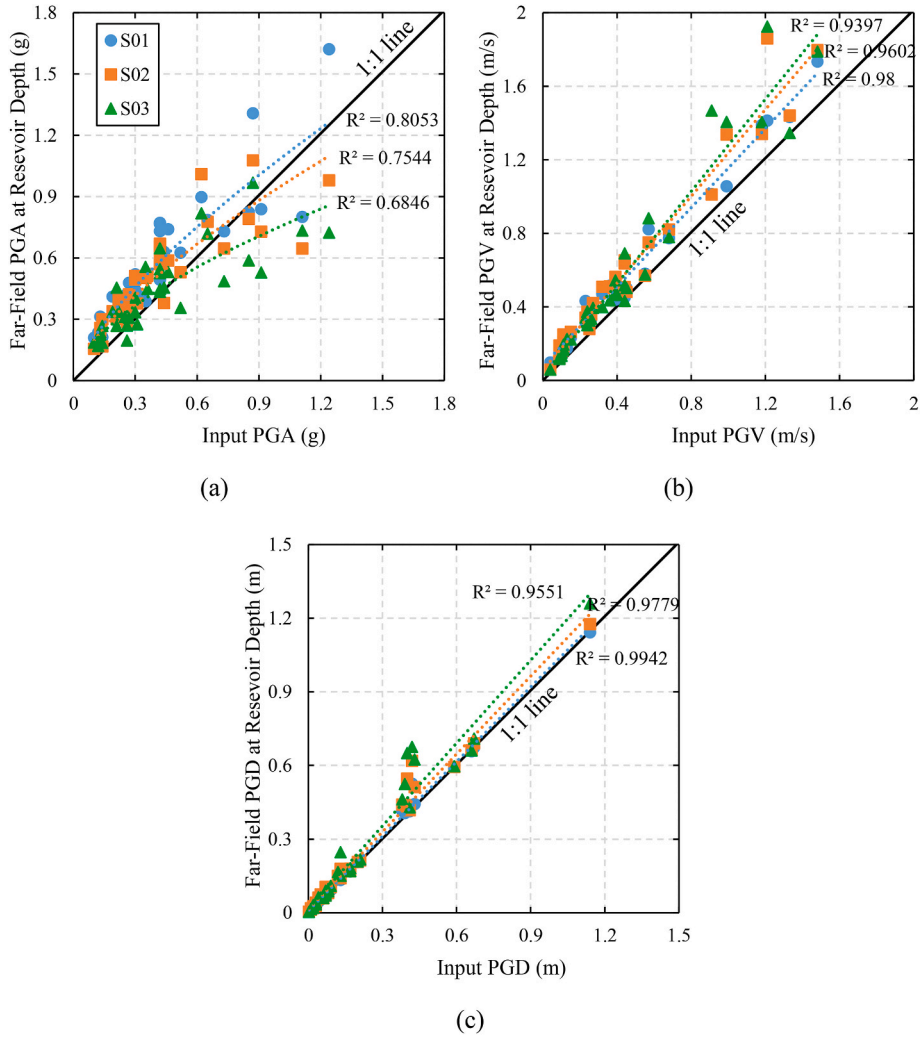

Fig. 7. Soil profile effects on the amplification/attenuation of (a) PGA, (b) PGV, and (c) PGD in the x-direction from bedrock to reservoir depth at far-field.

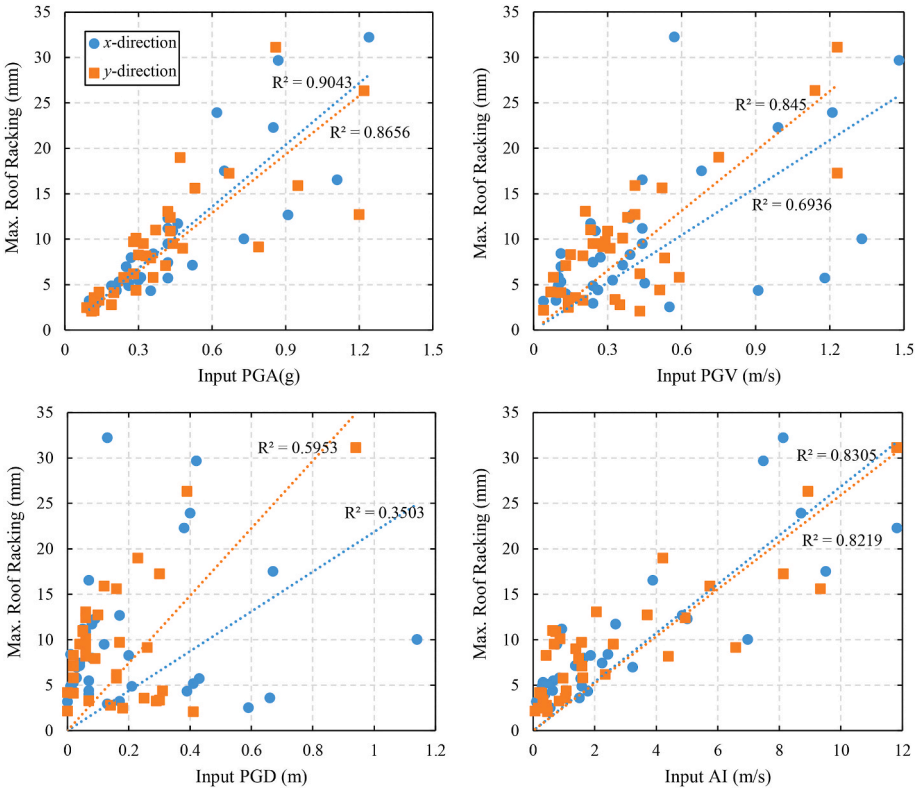

Fig. 8. Maximum roof racking displacement as a function of peak motion parameters for the case of R01_S01_D01_2D.

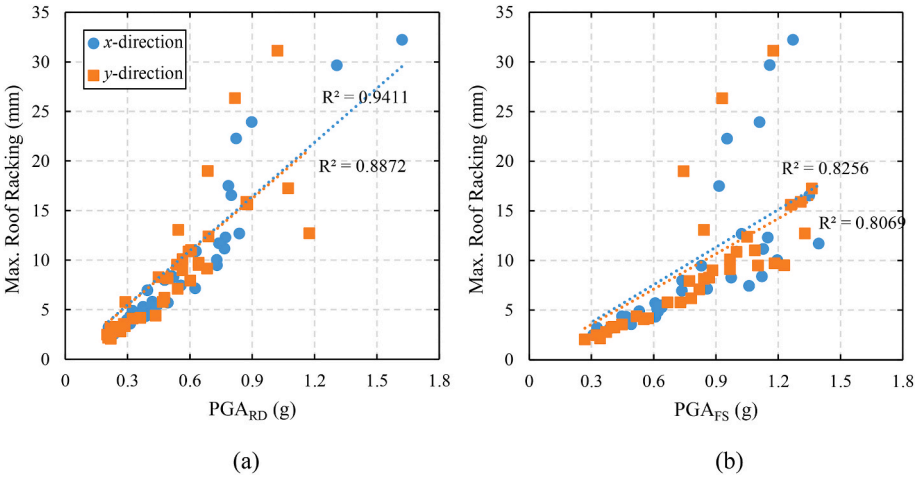

Fig. 9. Maximum roof racking displacement as a function of (a) far-field PGA at reservoir depth (PGA_{RD}) and (b) far-field surface PGA (PGA_{FS}) for the case of R01_S01_D01_2D.

Throughout the simulation, a constant downward gravitational acceleration of 9.81 m/s^2 was applied to all the model components. To mitigate initial numerical noise from sudden gravity application, a 1-s dynamic relaxation stage with a critical damping factor ($4\pi/T$) preceded each motion. Spot checks were conducted to ensure that no numerical noise remained after the dynamic relaxation phase and that the static demand magnitude and distribution were as expected. Initial conditions are achieved by a gravity turn-on procedure since the exact construction sequence is not known.

4.2. Reservoir structure

A box-shaped structure, with the dimensions listed in Table 2, was used while including structure-specific features. Based on typical structural configuration of real reservoirs, drop panels, column footings, and wall footings were represented in the model, as shown in Fig. 6. The reservoir's outer shell was modeled using four-node fully integrated shell elements with three through-thickness integration points. Two-node Hughes-Liu beam elements with 9 (3 × 3) through-thickness integration points were used for the columns. The column ends were offset by the thickness of the drop-panel or footing and a rigid nodal constraint was assigned between the column and the slab/roof. This would reflect the stiff zone that exists at the footing and drop-panel.

The nonlinear reinforced concrete material model, MAT-172, was employed [13]. MAT-172 (MAT_CONCRETE_EC2) is a material model available in the LS-DYNA material library that can represent plain

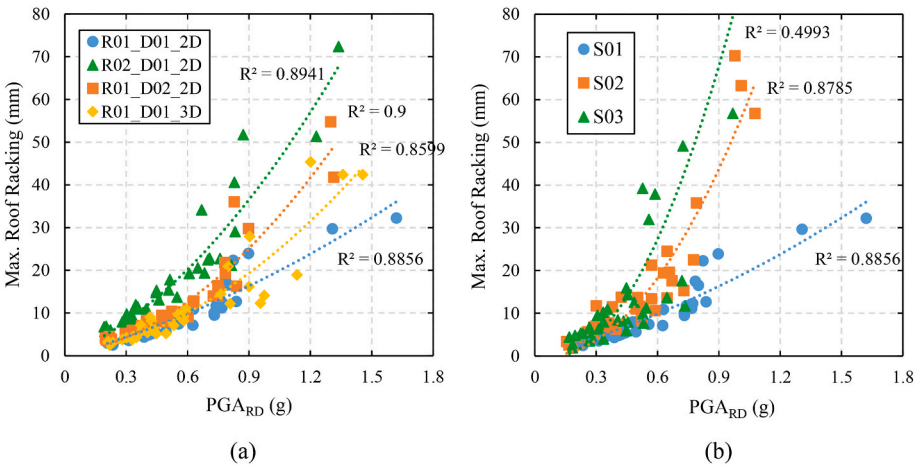

Fig. 10. Effects of (a) reservoir size, embedment depth, 3D motions for case of S01, and effects of soil profile for the case of R01_D01_2D on the maximum roof racking in the *x*-direction.

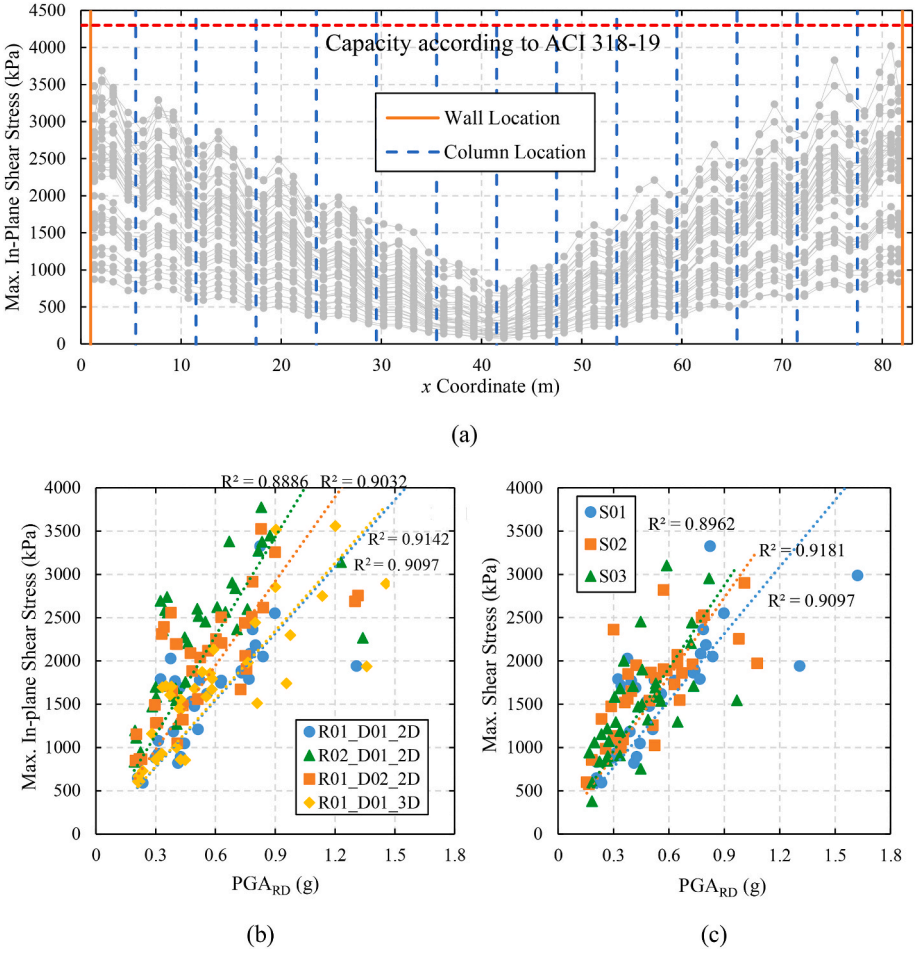

Fig. 11. Maximum in-plane shear stress in the roof slab: (a) distribution at the center from the south to the north wall for the case of R02_S01_D01_2D, (b) reservoir size, embedment depth, 3D motion effects for the case of S01, and (c) soil profile effects for the case of R01_D01_2D.

concrete only, reinforcing steel only, or a smeared combination of concrete and reinforcement. This model is available for shell and Hughes-Liu beam elements. The model includes concrete cracking in tension and crushing in compression as well as reinforcement yielding, hardening, and failure. The material properties of concrete were obtained according to the Mander et al. [27] confined/unconfined concrete material model. The steel reinforcement was considered to behave as elastic perfectly plastic capped at steel yielding strength. The material properties assigned in MAT-172 are listed in Table 6. A smeared combination of concrete and reinforcement was utilized with a steel reinforcement ratio provided in Table 2. Only 2 percent of viscous damping was applied, using the frequency-independent formulation, to all the structural parts because a nonlinear material with inherent hysteretic damping was already employed. Although ASCE/SEI 7–22 [21] permits

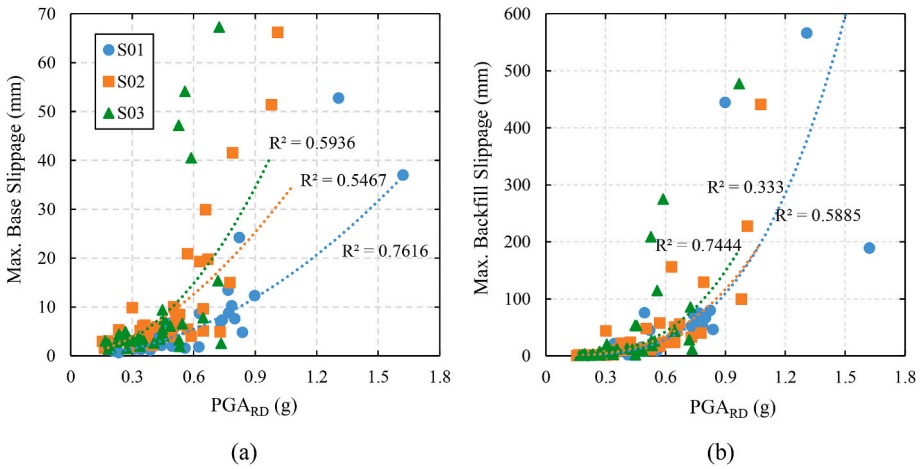

Fig. 12. Maximum (a) base slippage and (b) backfill slippage in the *x*-direction for the case of R01_D01_2D.

the slab to be idealized as a rigid diaphragm since span-to-depth ratio is less than 3, the slab stiffness was explicitly modeled to have a more accurate representation (i.e., semirigid modeling).

4.3. Stored water

In the study of AlKhatib et al. [14], three reservoir filling scenarios (full, half-full, and empty) were investigated experimentally and numerically. The full reservoir scenario was found to impose the greatest structural demands among the three cases. Additionally, given that reservoirs are typically operational and filled with water, this scenario reflects practical conditions. Consequently, only a full reservoir case was considered in this parametric study. A minimum freeboard, which is the clear distance between the maximum water level and roof, is typically provided to accommodate maximum vertical displacement of fluid sloshing during earthquake. When the reservoir is filled to the freeboard it is said to be operationally full. Several factors control the design of the freeboard such as the reservoir size, the structure importance, and the site seismic hazard. Since different reservoir sizes, soil profiles, and seismic intensities were investigated, a constant freeboard was used for all models for simplicity and to make later comparison of results feasible. Therefore, the water height was set at 6.4 m, leaving a freeboard distance of 1.6 m for all cases.

The ALE formulation was employed to model the stored water. Previous studies [17,28] have validated the capability of the ALE formulation in capturing the dynamic behavior of water by comparing its predictions against experimental results. The Grüneisen equation of state was used to describe the water material, with properties listed in Table 7. No damping was assigned to the water.

The interface between the reservoir's outer shell (walls, slab, and roof) and the water was established using a coupling algorithm available in LS-DYNA. The coupling algorithm was validated against the FSSI centrifuge experiments [14], with example results presented in Fig. 2. Several studies [29] have examined the interaction of water waves with vertical cylinders similar to columns. However, no coupling was established between the stored water and the columns in this study, as the system did not meet the conditions under which this interaction would be important (e.g., column size, spacing, circular shape, etc.).

5. Effect of key parameters

This section evaluates the effects of different parameters on the seismic response of reservoirs when subjected to shaking. The response is evaluated by tracking the changes in behavioral aspects that include: (1) roof racking displacement, (2) slippage of base and overlaying soil, (3) dynamic earth pressures, (4) seismic demands on the walls and columns, and (5) stored water hydrodynamic pressures. Trend lines are added to data plots to provide a general sense of the response variation.

5.1. Seismic wave propagation

It is well established in the literature that site stiffness significantly impacts the seismic waves propagating from the bedrock to the structure, a relationship that can be assessed through site response analyses. Peak ground motion parameters, such as peak ground acceleration, velocity, and displacement (PGA, PGV, and PGD, respectively) are commonly used metrics in the field of seismic design and earthquake engineering. For instance, in the seismic design of conventional underground structures, these parameters are extensively used in closed-form and simplified solutions [1]. Fig. 7 illustrates the comparison of PGA, PGV, and PGD of the input motion with those recorded at the far-field (near model boundary) at a depth corresponding to the reservoir base (denoted as PGA_{RD}, PGV_{RD}, and PGD_{RD}). In Fig. 7 (a), PGA_{RD} is generally higher than the input PGA. However, for input PGAs exceeding 0.6g, PGA_{RD} is lower, particularly for the soft site S03. This reduction is attributed to soil yielding at high intensity shaking, which attenuates vertically propagating waves, thus decreasing PGA_{RD}. Conversely, the stiffest site, S01, exhibited the highest PGA_{RD}, as it transmits seismic waves with amplification or minimal attenuation compared to softer sites. Both PGV_{RD} and PGD_{RD} were found to be slightly higher than the input motion values, with the highest recorded for the case of soft site S03, as shown in Fig. 7(b) and (c), respectively.

5.2. Roof racking

The roof racking was evaluated against four different input motion parameters (at the bedrock) in each of the *x* and *y* directions: PGA, PGV, PGA, and Arias Intensity of the ground motion (AI). For example, the input PGA in the *x*-direction was plotted against the maximum roof racking along the *x*-direction, and similarly for the *y* direction. Fig. 8 shows the correlations between the various ground motion parameters and the maximum roof racking displacement for the case of R01_S01_D01_2D. PGA demonstrated the strongest correlation, with an R^2 value of approximately 0.9, while PGD showed the weakest correlation. PGV and AI exhibited a good correlation with maximum racking displacements. The strong correlation of PGA shows that, unlike other underground structures [1], the kinematic interaction of the soil with the reservoir is not as significant as the inertia of the roof and overlaying soil, which primarily drives the demands on the reservoir. It also suggests that the reservoir has a relatively stiff structure, primarily controlled by the spectral accelerations of low periods, such as PGA.

A similar plot of maximum roof racking against the far-field PGA

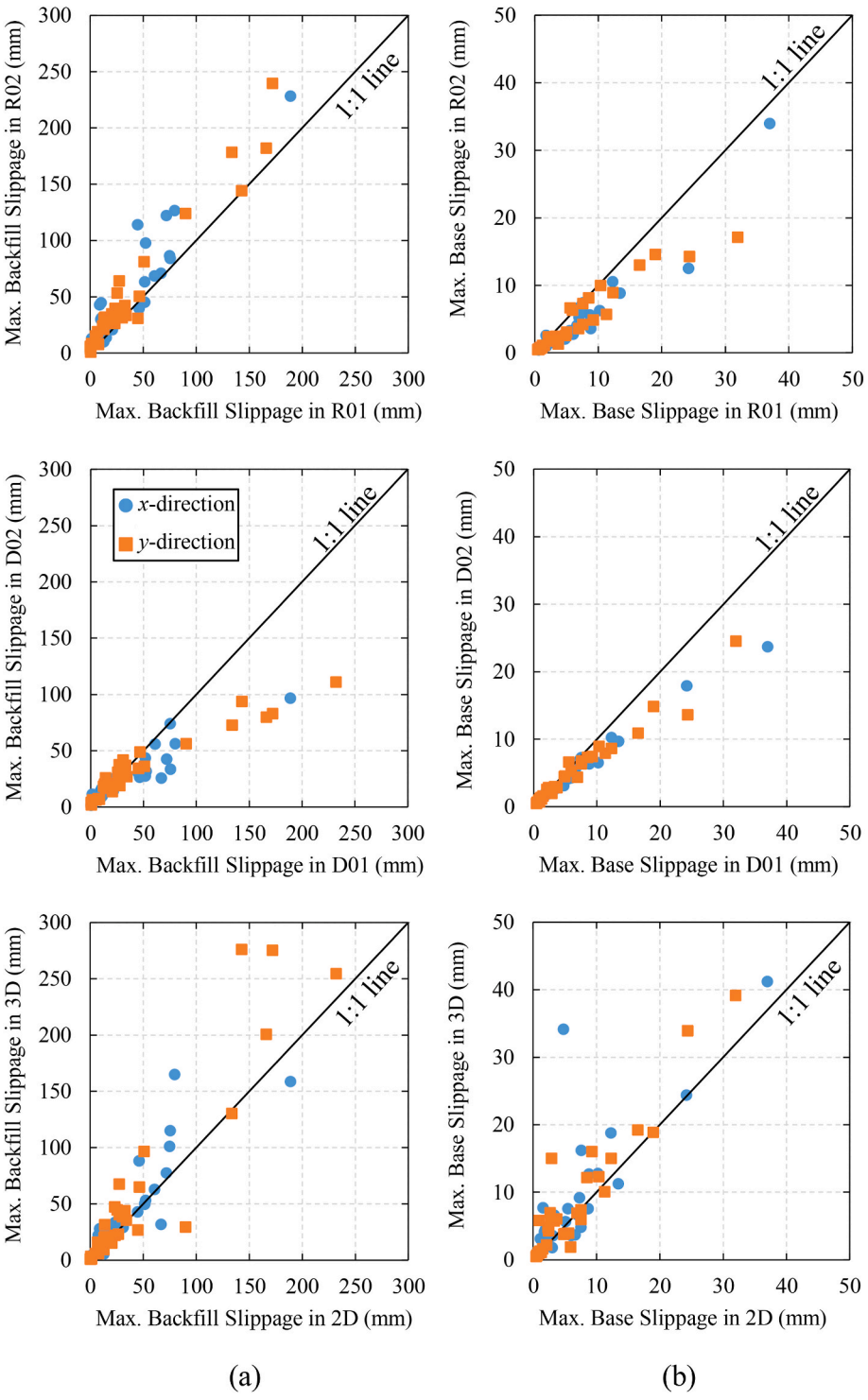

Fig. 13. Effects on (a) maximum backfill slippage, and (b) maximum base slippage.

near model boundary at the ground surface (PGA_{FS}) and at a depth corresponding to the reservoir base (PGA_{RD}) is provided in Fig. 9. A stronger correlation was observed with the PGA_{RD}, with an increase in R^2 reaching approximately 0.94. This is attributed to the reduction in scatter caused by site response effects when considering the motion at the reservoir depth as a reference instead of the input motion. Nevertheless, scatter in the data can be expected due to ground motion variability and nonlinear site response. Therefore, the strong correlation with racking displacements suggests that PGA_{RD}, which can be readily obtained using a site response analysis, could serve as a suitable ground motion parameter for estimating racking displacement and seismic demands.

The effects of reservoir size, embedment depth, and vertical motion inclusion are illustrated in Fig. 10(a). The increased roof inertia and span distance between supporting walls of R02, compared to R01, caused a significant increase in roof racking displacements. Similarly, increasing the embedment depth increased the mass, and thus the inertial forces generated at the roof, which in turn increased the racking. The inclusion of vertical motion didn't cause significant change to the roof horizontal racking displacement, as it acts perpendicular to it.

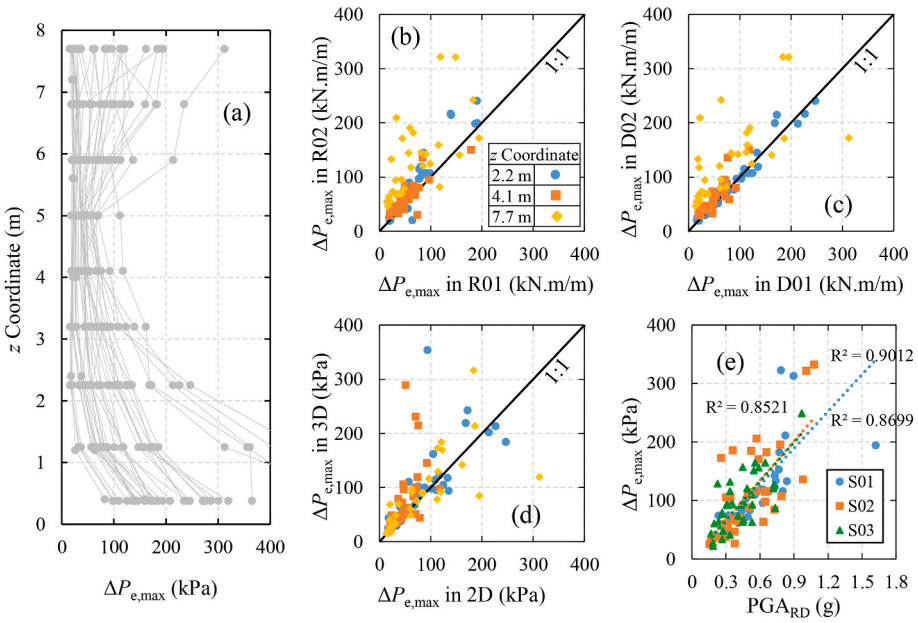

Fig. 14. $\Delta P_{e,max}$ at the middle of the south wall: (a) vertical distribution (R02_S01_D01_2D), and the effects of (b) reservoir size (S01_D01_2D), (c) embedment depth (R02_S01_2D), (d) 3D motions (R02_S01_D01), and (e) soil profile (R01_D01_2D).

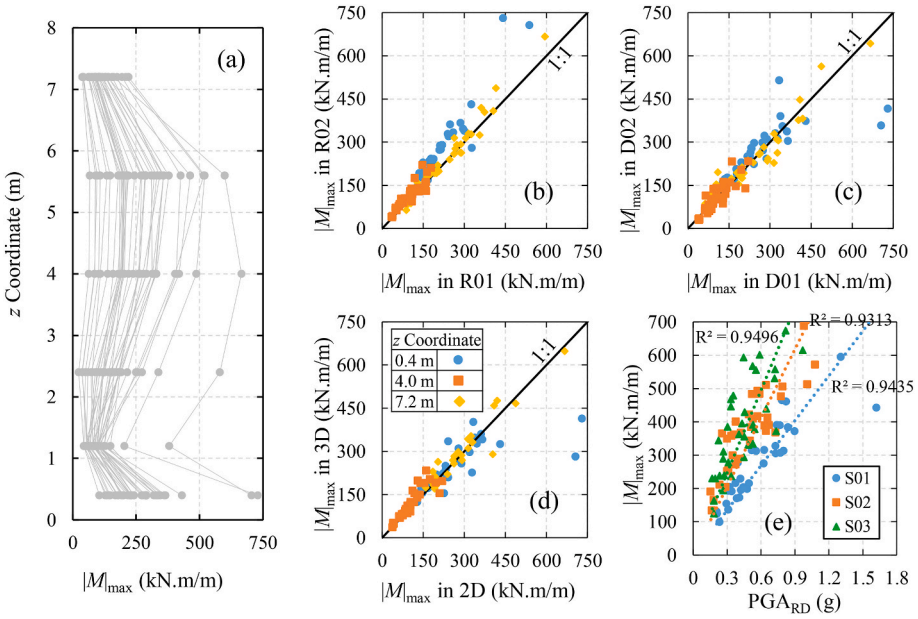

Fig. 15. $|M|_{max}$ at the middle of the north wall: (a) vertical distribution (R02_S01_D01_2D), and the effects of: (b) reservoir size (S01_D01_2D), (c) embedment depth (R02_S01_2D), (d) 3D motions (R02_S01_D01), and (e) soil profile (R01_D01_2D).

However, an increase was observed for cases with high PGA_{RD} (>1.0g), which may be attributed to the increased yielding in the resisting elements caused by the inclusion of the vertical motion component. As illustrated in Fig. 10(b), softer sites caused higher racking mainly due to the lesser passive resistance provided to the reservoir during shaking.

The roof's racking shape was found to be non-uniform, with minimal displacement near the resisting walls and peaks at the center. Fig. 11(a) illustrates the computed maximum in-plane shear stress distribution along a north-south line that cuts the roof at its center. The maximum stress levels gradually increased from the center towards the supporting walls, with minor drops observed at the columns' locations. This indicates the diaphragm behavior of the roof and the minimal lateral resistance provided by the columns when compared to that provided by the side walls, which is consistent with the findings of AlKhatib et al. [14]. Similar to the effect on roof racking, increasing the reservoir size and embedment depth, as well as the presence of softer sites, were found, in Fig. 11(b) and (c), to increase the maximum in-plane shear stresses. The effect of including the vertical component of the motion in the analysis had almost no impact on the in-plane shear stresses. The vertical motion therefore may increase the roof racking displacement at high intensity motions due to its weakening effects on the vertical resisting elements but would not increase the roof in-plane stresses, owing to its perpendicular orientation to the racking plane. On the other hand, the vertical deflection of the roof was found to increase when including vertical motions.

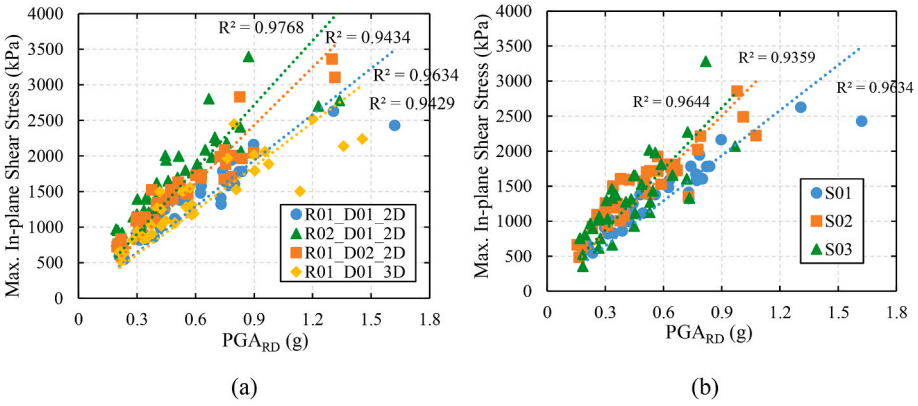

Fig. 16. Maximum in-plane base shear stress at the middle of the east and west walls: (a) reservoir size, embedment depth, and 3D motion effects, and (b) site effects.

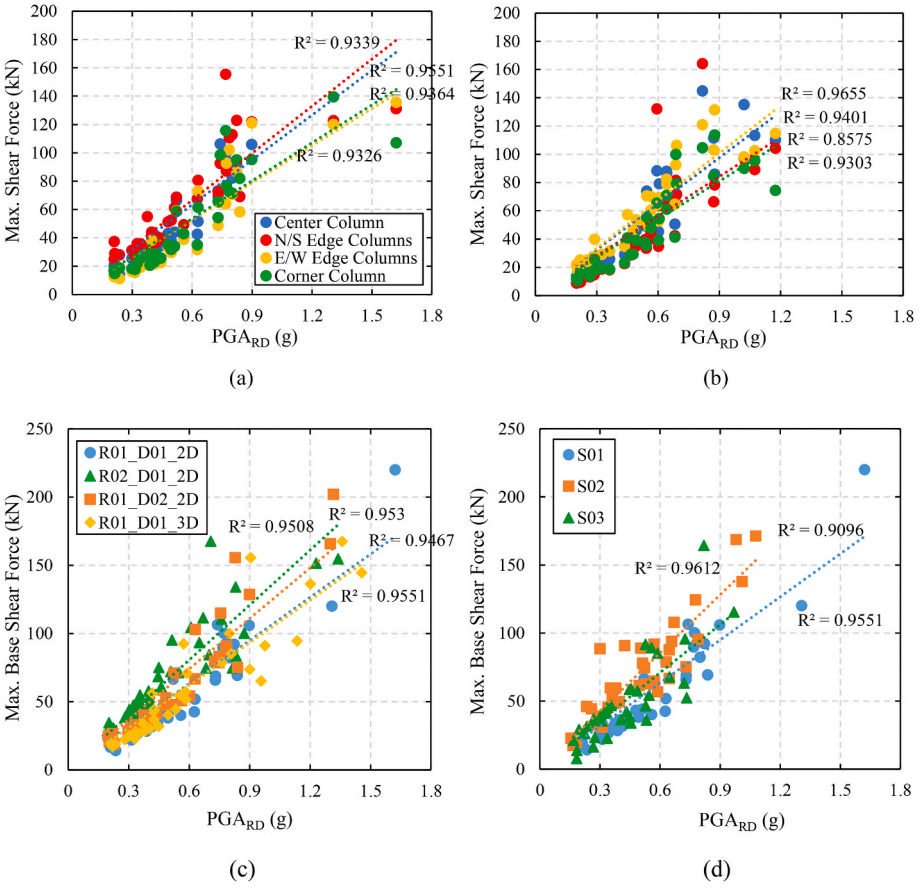

Fig. 17. Maximum shear force at the base of the columns in the (a) *x*-direction and (b) *y*-direction for R01_S01_D01_2D, (c) effects of reservoir size, embedment depth, and 3D motions (S01), and (d) site profile effects (R01_D01_2D).

5.3. Base and overburden slippage

During shaking, seismic forces are transmitted to the system through the soil-structure and structure-fluid interfaces. At soil-structure interface, there exists a finite frictional capacity which prevents the relative displacement of neighboring soil and structure elements through generating counter tangential forces. The frictional capacity is determined by the interface friction coefficient and the applied normal stresses. At high intensity shaking, the available frictional capacity may be exceeded causing soil-structure relative displacements, also known as slippage. Slippage was observed to occur mainly between the base of the reservoir and the underlaying soil, as well as between the roof and the overlaying backfill soil. Fig. 12 shows the variation of the maximum slippage with respect to PGA$_{RD}$ in the case of R01_D01_2D with the three different sites S01, S02, and S03. For all cases, slippage was almost negligible at low PGA (<0.3g), progressively increasing nonlinearly with increasing PGA$_{RD}$. The slippage of the backfill soil was observed to be higher than the slippage observed at the reservoir base since the available normal stress is higher at the base. Softer sites were observed to increase the slippage in general due to the lesser passive resistance provided to the reservoir.

Fig. 13 compares the base and backfill soil slippage for different cases of reservoir size, embedment depth, and motion type. Increasing reservoir size was found to increase the overlaying backfill slippage mainly

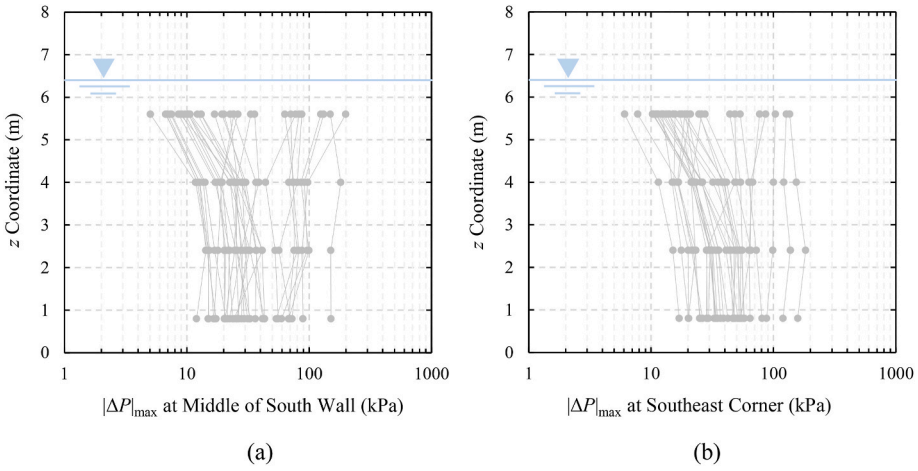

Fig. 18. Vertical distribution of $|\Delta P|_{max}$ at (a) middle of the north wall, and (b) northeast corner for the case of R01_S01_D01_2D.

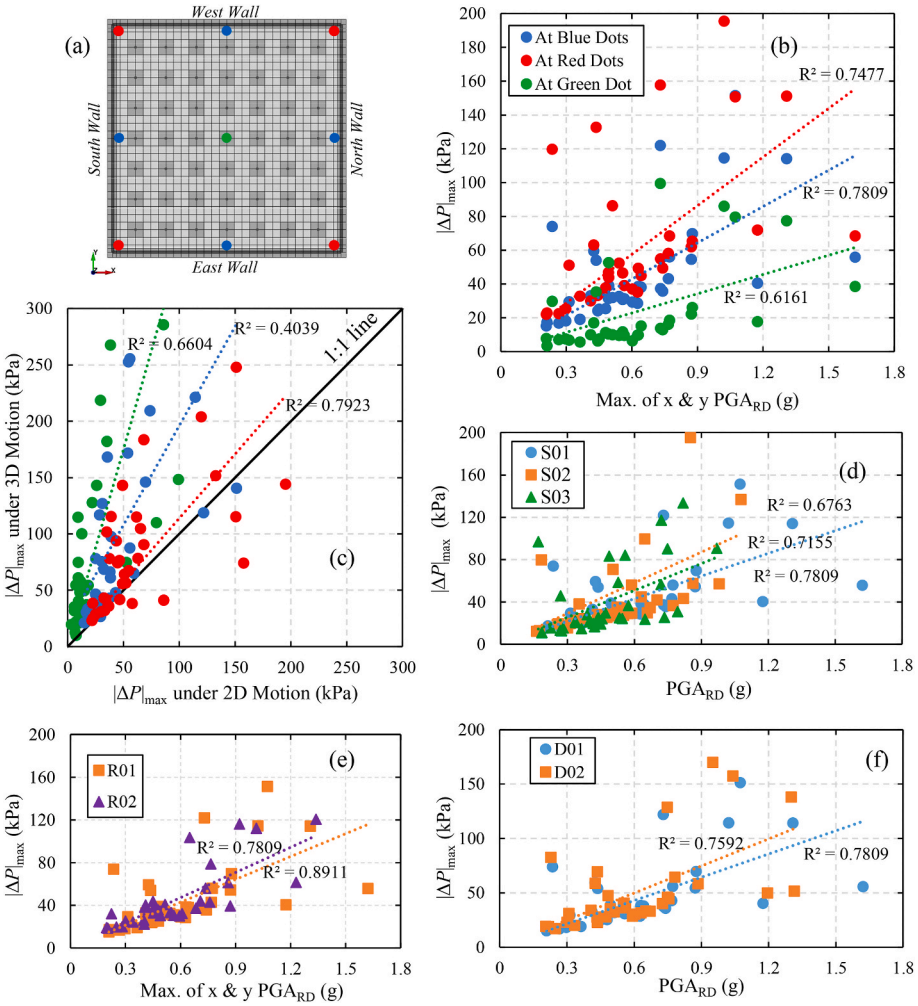

Fig. 19. Hydrodynamic pressures (R01_S01_D01_2D): (a) plan-view showing the locations of interest, (b) peak hydrodynamic pressures and the effect of (c) 3D motions, (d) site profile, (e) reservoir size, and (f) embedment depth near the edge (blue dots).

due to the higher roof racking of R02, compared to R01, as discussed earlier. On the other hand, base slippage was observed to decrease when increasing the reservoir size. The larger footprint of R02 provided a greater resisting interface area, thereby reducing slippage. Two cases of embedment depth, D01 and D02, were also compared in terms of maximum slippage, as shown in Fig. 13. It was found that increasing the embedment depth would reduce slippage due to the corresponding increase in the normal stresses at the interface between the reservoir and the soil. Finally, the influence of including vertical motion on base and backfill slippage was observed to lack a clear trend of increase or decrease. The normal stresses existing at the soil-structure interface, which is generated from the system weight, can fluctuate during shaking

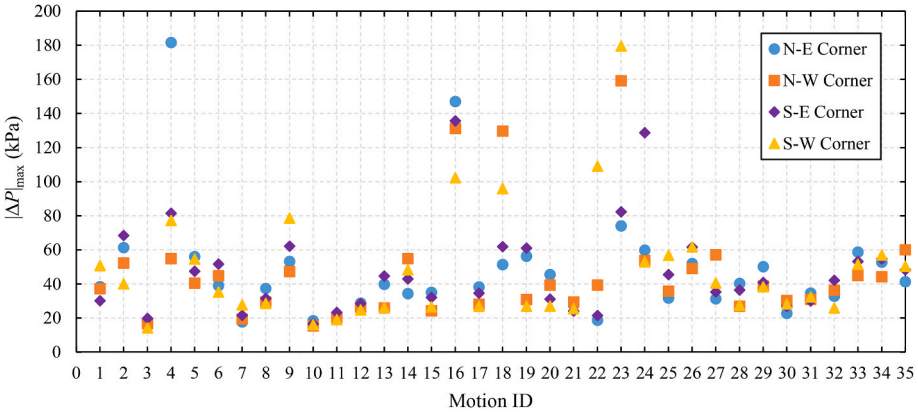

Fig. 20. Distribution of peak hydrodynamic pressures at the bottom of the four corners (R01_S01_D01_2D case).

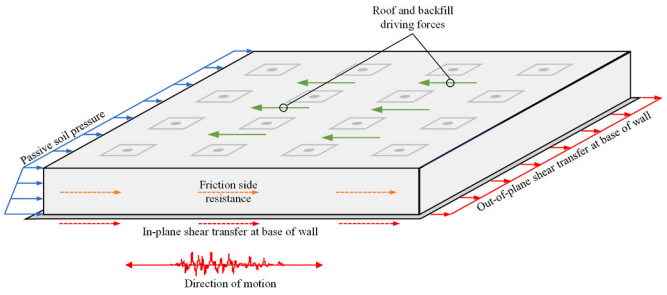

Fig. 21. Mechanisms for lateral load resistance.

due to vertical accelerations. The change in the slippage, compared to a case with no vertical motion, would be determined by how the motion's vertical component interacts with the other two horizontal motion components.

5.4. Dynamic earth pressures

The vertical distribution of peak earth dynamic pressures ($\Delta P_{e,max}$) at the south wall is provided in Fig. 14(a) for the case of R02_S01_D01_2D. Earth pressures were observed to be the highest near the bottom and top of the reservoir, with the lowest pressures observed at mid-height where the wall exhibits greater flexibility due to its structural configuration. Fig. 14(b) demonstrates that R02 case exhibit higher earth pressure compared to R01, especially near the top of the reservoir, primarily due to the increased racking displacements caused by the larger roof inertia and span distance between supporting walls. Fig. 14(c) shows that a greater embedment depth (D02) results in higher earth pressures, especially at the top, owing to the increased mass and subsequent inertial forces. As illustrated in Fig. 14(d), including the vertical component of the motion caused variations in the earth pressure distribution; however, no consistent trend was observed, suggesting that the impact of vertical motion on earth pressures is complex and likely influenced by multiple factors, including soil-structure interaction and the dynamic characteristics of the motion itself. Finally, the soil profile was shown in Fig. 14(e) to have minimal effects.

5.5. Seismic demands on walls

Reservoir walls were found to resist most of the seismic demands through in-plane shear [14]. They also experience dynamic out-of-plane shear and bending moments due to imposed dynamic earth pressure and roof racking, predominantly in the vertical direction, except near the corners where a two-way load transfer mechanism prevails. Fig. 15(a) illustrates the vertical distribution of the absolute maximum bending moment ($|M|_{max}$) at the middle of the north wall for the case of R02_S01_D01_2D. High bending moments were observed near the bottom and at around two-thirds of the wall height, attributed to the near fixity provided by the wall footing at the bottom, while the roof slab acted as a diaphragm.

Additionally, Fig. 16 compares the maximum base in-plane shear stress at the middle of the east and west walls against PGA_{RD} for different cases. From Fig. 15(b) and 16(a), it is evident that increasing the reservoir size results in an increase in wall dynamic demands. An increase in in-plane shear with no significant change in bending moment was observed with increased embedment depth, as shown in Fig. 16(a) and 15(c), respectively. As illustrated in Fig. 15(d) and 16(a), including the vertical motion had minimal impact in terms of in-plane shear and bending moment as it acts parallel to the walls. According to Fig. 15(e) and 16(b), softer soil profiles caused an increase in wall dynamic demands.

5.6. Seismic demands on columns

Compared to their primarily role in carrying the weight of the roof, the columns' role in resisting lateral loads is rather insignificant. Nevertheless, during earthquakes, roof racking displacement imposes additional cyclic stresses on the columns that should be accounted for in the design. This was evident after the Mw 6.6 San Fernando Valley Earthquake in 1971, where sever damage occurred at the column ends of Balboa Reservoir [5]. Fig. 17(a) and (b) show the maximum base shear in both directions experienced by the columns located near the reservoir's center, edges, and corners. While columns are often moment-controlled, base shear was used as a metric of comparison since it is commonly used in design codes (e.g., ASCE 7–22). Though not included in this study, in scenarios where the reservoir has varying floor elevations, reporting bending moment alone can be misleading. Base shear provides a more consistent measure of the distribution of seismic resistance across columns of varying heights (if exist) by avoiding the distortion that height differences introduce when using bending moments.

Center columns was found to experience the highest base shear, while corner columns experience the lowest. High shear is experienced by the edge columns in the direction perpendicular to the edge to which they are next. This can be attributed to the racking shape of the roof which is minimum near the resisting walls parallel to the motion and maximum at the center. Impact trends of the studied key parameters were similar to those observed for the walls as shown in Fig. 17(c) and (d).

5.7. Stored water hydrodynamic pressures

The presence of stored water produces additional seismic demands

Table 8
Summary of structural failure cases.

Reservoir Size	R01												R02												Failed cases
Soil Profile	S01				S02				S03				S01				S02				S03				
Embedment Depth	D01		D02		D01		D02		D01		D02		D01		D02		D01		D02		D01		D02		
Type of Motion	2D	3D	2D	3D	2D	3D	2D	3D	2D	3D	2D	3D	2D	3D	2D	3D	2D	3D	2D	3D	2D	3D	2D	3D	
Motions that caused failure	0	0	0	0	0	0	0	0	0	0	1	3	0	0	0	2	2	2	3	5	2	1	4	3	28

due to its interaction with the reservoir structure through convective sloshing and impulsive hydrodynamic pressure [17]. While an empty reservoir might be the governing case in static design conditions, during earthquakes, presence of water was found to cause increased demands [14]. Fig. 18 shows the vertical distribution of peak hydrodynamic pressures ($|\Delta P|_{max}$) at the north wall for the case of R01_S01_D01_2D. Maximum dynamic pressures are observed to occur near the bottom of the reservoir, highlighting the predominant impulsive nature of water hydrodynamic response. Fig. 19 depicts the peak hydrodynamic pressures computed at the bottom of the reservoir near the center, edges, and corners. Fig. 19(b) shows that the corners experience the highest pressures inside the reservoir while the center experiences the lowest. This discrepancy arises because corners are impacted by acceleration generated in both neighboring walls, resulting in amplified hydrodynamic pressures. Fig. 20 further demonstrates that even among the four corners, different pressures are experienced, with the peak pressure potentially occurring at any corner depending on the resultant motion direction.

No significant increase in dynamic water pressure was observed with increasing reservoir size, as demonstrated in Fig. 19(e). This observation aligns with the theoretical expectation for large-scale reservoirs, where the concept of an infinite medium becomes applicable. As a result, impulsive dynamic pressures exhibit minimal sensitivity to further increases in reservoir horizontal dimensions unless accompanied by a corresponding increase in water height. Moreover, the convective sloshing effects are primarily governed by the natural period of the water mass. In large reservoirs, the horizontal dimensions are significantly greater than the height, leading to a longer fundamental period for the stored water. This extended period, which coincides with low spectral acceleration of typical motions, means the reservoir rarely reaches resonance conditions where sloshing effects would be most pronounced. Therefore, while impulsive pressures remain relatively stable, the contribution of convective sloshing to the overall dynamic pressure is minimal, unless low-frequency motions are imposed (e.g., subduction zone motions). As shown in Fig. 19(c), the water pressures at all locations inside the reservoir were found to generally increase due to the vertical accelerations. This can be attributed to the fact the vertical accelerations would add to the static weight of the water thus increasing water pressure. Fig. 19(d) and (f) demonstrate that increasing embedment depth and softer sites would not have significant impact on water hydrodynamic pressures.

6. Mechanism of seismic load transfer

During an earthquake, the reservoir experiences lateral loads from soil pressures acting on the walls and accelerations transmitted to the structure when the soil beneath it moves. These loads are resisted by a combination of different types of resistance as illustrated in Fig. 21. The driving force is depicted as an inertial force that is of the same magnitude and opposite direction to the force transmitted to the structure by the soil at the base and sides. Of the effective inertial force, more than ninety percent of the load passes through the shear walls parallel to the driving force down to the floor slab to be resisted by friction against the soil below. For example, in the case of bidirectional motion, the south-north component of the driving force is mostly resisted by the east and west walls, and the west-east component of the driving force is mostly resisted by the north and south walls. The roof is considered to act as a diaphragm in its plane, spanning between supporting walls. Shear force gradually increases from the center of the span towards the ends at the supports, reflecting the addition of inertial load.

7. Failure mechanism

As described earlier, a nonlinear reinforced concrete material model was utilized for the reservoir structure, leading to 28 out of the 840 cases resulting in reservoir failure under strong ground motions. Table 8

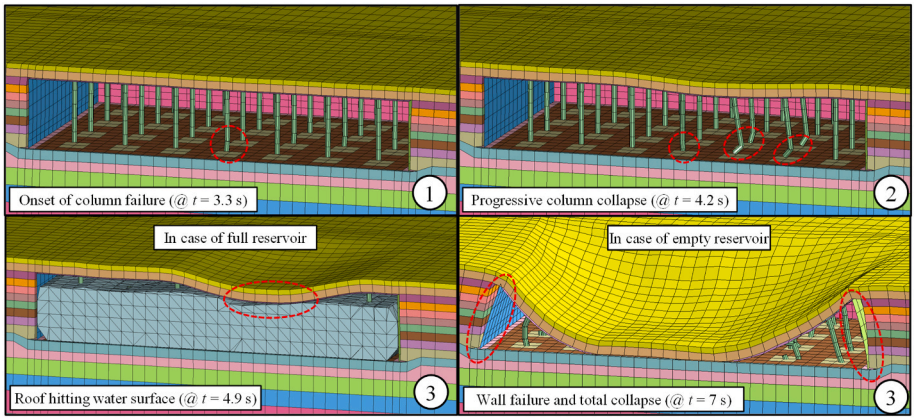

Fig. 22. Snapshots from the FE models of the failure stages for the cases of full and empty reservoirs (screenshots 1 and 2 are for both cases – water is hidden for clarity).

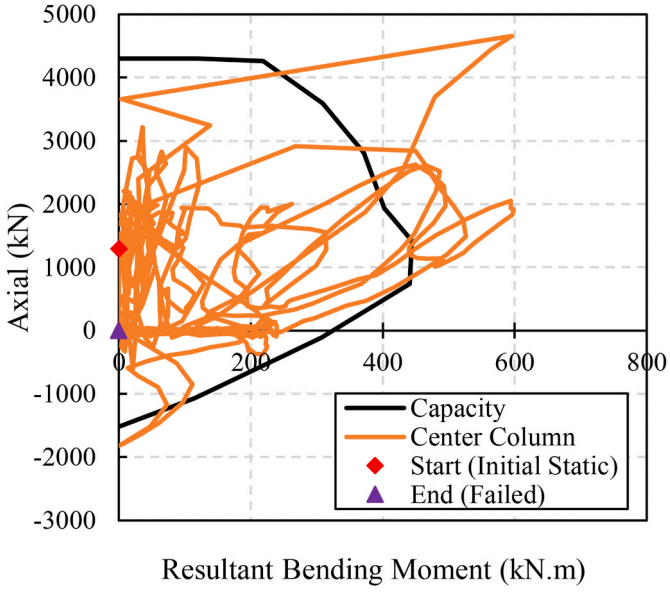

Fig. 23. P-M interaction curve at the bottom of the center column (R01_S03_D02_3D_M18 case).

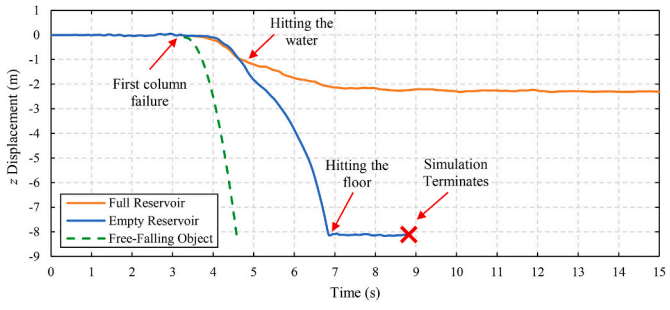

Fig. 24. Vertical displacement of the roof near the point of failure initiation.

illustrates that the likelihood of failure increased with larger reservoir size, softer site conditions, greater embedment depth, and 3D motion, as these parameters were shown to increase the overall demands. To analyze the failure mechanism, Fig. 22 presents snapshots of the failure stages for the case of R01_S03_D02_3D under M18 motion. A scenario of an empty reservoir for that specific case was also added in the investigation. The structural collapse was initiated when one of the center columns failed near the base due to high lateral demands. Fig. 23 shows that the axial-moment (P-M) interaction diagram of the column exceeded its capacity according to ACI 318-19 [30] causing the failure. The failure of the first column was then followed by progressive failure of the neighboring columns which had been already weakened by the cyclic loading preceding the failure. Fig. 24 shows the vertical displacement of the roof near the point where failure was initiated. The curve for a free-falling object is added for reference. In the case of the full reservoir and once the roof impacted the water surface, the buoyancy of water prevented, or at least delayed, the subsequent collapse. In the case of the empty reservoir, a total collapse was reached. The rapid and excessive roof subsidence, due to progressive column failure, induced the roof to act as a 2-way membrane, engaging in a catenary action that pulled the exterior walls inwards, leading to their failure.

Although the model cannot fully capture the consequences following a failure, it is understood that the development of wide cracks or structural failure in the reservoir walls or slab can lead to significant water loss. Reservoirs are typically designed with drains at the sides and bottom, which can exacerbate the loss of water in the event of structural failure. In cases where the reservoir is situated on leveled ground, as in this study, water would likely seep into the ground due to gravity. While this might mitigate immediate flooding, the critical issue remains the loss of water, which is vital for maintaining active water supply and firefighting capabilities following an earthquake. Conversely, when reservoirs are located near slopes or elevated terrains, the risk becomes more severe. Structural failures can lead to sudden breaches, causing water to flow under pressure from the reservoir. This could result in significant leakage and potential flooding of downstream areas.

8. Conclusions

Buried water reservoirs are a relatively new class of structures, playing a crucial role in many US cities for storing and supplying water, yet there is a notable gap in research regarding their seismic performance. Reservoir failure would not only come with a great cost of repairs but also poses significant risks to nearby communities. There have been cases of seismic collapse or costly retrofits due to the lack of well-established seismic design technique for this type of structure. Advancements in the fluid-structure-soil interaction (FSSI) modeling are essential for understanding and leveraging the behavior of buried reservoirs. This would help advance their performance-based design approach, which is more favorable and adaptable than traditional code-based design approaches.

A large-scale numerical parametric study was presented in this paper to investigate the seismic FSSI behavior of buried reservoirs. The study investigated key parameters that included reservoir size, embedment depth, soil profile, and ground motion variability yielding a total

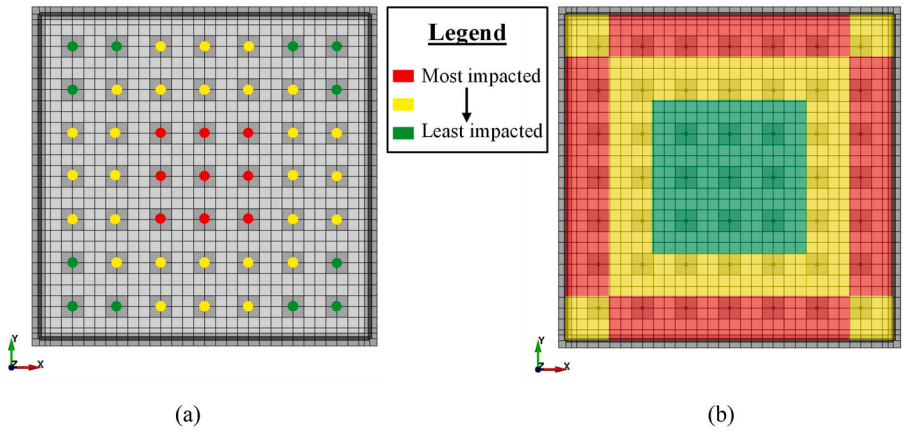

Fig. 25. A rough diagram highlighting the most and least impacted (a) columns and (b) areas of the roof slab during earthquakes.

Table 9
Summary of the effects of the investigated parameters on the reservoir seismic response.

Reservoir Response	Parameters				
	Ground motion parameters	Softer Soil Profiles	Increase in reservoir size	Increase in embedment depth	3D motion compared to 2D
Roof racking	- PGA has strong correlation	Increases	Increases	Increases	Increases at high PGA
Base slippage	- PGV and AI have good correlation	Increases	Decreases	Decreases	Changes, but no clear trend
Backfill slippage	- PGD has weak correlation	Almost no effect	Slightly Increases	Decreases	Changes, but no clear trend
Roof dyn. deflection		Increases	Almost no effect	Increases	Increases
Water dyn. pressure		Almost no effect	Almost no effect	Slightly Increases	Increases
Wall moment		Increases	Increases	Demands slightly shift downwards	Almost no effect
Wall in-plane shear		Slightly Increases	Increases	Increases	Almost no effect
Column base shear		Increases	Increases	Increases	Almost no effect
Earth dyn. pressure		Increases near roof; decreases near bottom	Increases	Increases near roof	Changes, but no clear trend
Roof in-plane shear		Increases	Increases	Increases	Almost no effect

number of 840 different cases/simulations. A summary of the key behavior is presented in Table 9 and described as follows.

- The PGA was found to have the strongest correlation to the reservoir response (e.g., racking deformation, stress demand, etc.). This indicates that the inertia/mass of the roof is the main source of demand and not the soil kinematic interaction which dominates the behavior of other conventional underground structures (e.g., deep tunnels).
- Considering the vertical component of the motions (3D motion) was found to increase the water pressures and vertical deflection of the roof.
- The increase in the embedment depth was found to decrease the base and backfill slippage and increase the roof racking, vertical deflection of the roof, and column base shear.
- Increasing the reservoir size resulted in an increase in the roof racking, columns and roof shear demands, and earth pressures.
- Soft sites increased the demands on all structural elements as they provide less passive confining resistance to the reservoir racking.
- The parametric study showed the areas inside the reservoir which are most and least impacted by the earthquake. For example, as shown in Fig. 25, columns at the center experience the highest base shear, and the edge of the roof was found to exhibit the highest in-plane shear demands.

Based on the parametric study results, the authors propose the following implications and recommendations for design practice.

- The reservoir response is shown to be highly complex and 3D in nature. Therefore, conducting a high-fidelity numerical model that includes the FSSI is the best approach to tackle this problem. A 2D plane strain simplification would be inappropriate for the seismic design of reservoirs.
- The reservoir response is highly influenced by ground motion PGA and the inertia of the roof. Thus, the simplified kinematic interaction methods (e.g., pseudo-static analysis) used for the seismic design of conventional underground structures are not applicable for reservoirs and may underestimate the demands.
- Softer sites were shown to provide insufficient passive confinement to reduce slippage. Therefore, a stiff, well compacted backfill is recommended in the vicinity of the reservoir. Greater caution should be given for cases of reservoir near a slope.
- 3D input motions should be used in the model to account for the more critical condition of bidirectional loading and the added weight due to the vertical motion component.

This extensive parametric study leveraged advanced numerical models validated against well-instrumented centrifuge model tests and expanded them to shed light on the intricate dynamics of buried water

reservoirs under seismic forces, unraveling key insights into their structural behavior. By investigated real-world field scenarios of peak ground acceleration, effects of 3D motions, embedment depths, reservoir sizes, and soil characteristics, the study provided a more nuanced understanding of the challenges and vulnerabilities these vital structures face during earthquakes. Nevertheless, further research is needed to address critical gaps in literature. Reservoirs near slopes, presence of high-water table, and ground susceptible to liquefaction are examples of cases yet to be investigated. With this acquired knowledge, engineers and policymakers would be better equipped to develop robust seismic design strategies, ensuring the resilience and safety of buried reservoirs for the communities they serve.

Data availability

Data will be made available upon reasonable request to the corresponding author.

CRediT authorship contribution statement

Karim AlKhatib: Writing – original draft, Visualization, Validation, Software, Investigation, Formal analysis, Data curation. **Youssef MA. Hashash:** Writing – review & editing, Supervision, Project administration, Funding acquisition, Conceptualization. **Katerina Ziotopoulou:** Writing – review & editing, Supervision, Project administration, Funding acquisition, Conceptualization.

Declaration of competing interest

The authors declare that they have no known competing interests that could have appeared to inflence the work in this paper.

Acknowledgments

The authors gratefully acknowledge the funding provided by the National Science Foundation under grants CMMI-1763129 and CMMI-1762749. Any opinions, findings, conclusions, or recommendations expressed in this paper are solely those of the authors and do not necessarily reflect the views of the National Science Foundation.

References

[1] Hashash YM, Hook JJ, Schmidt B, John I, Yao C. Seismic design and analysis of underground structures. Tunn Undergr Space Technol 2001;16(4):247–93. https://doi.org/10.1016/S0886-7798(01)00051-7.
[2] Wang J-N. Seismic design of tunnels: a simple state-of-the-art design approach. Parsons Brinckerhoff Quade & Douglas, Inc.; 1993.
[3] Kawashima K. Seismic design of underground structures in soft ground: a review. Presented at the international symposium on tunneling in difficult ground conditions. 1999.
[4] Kenmir Russell C. Concrete reservoir design. J Am Water Works Assoc 1968;60 (10):1181–94. https://doi.org/10.1002/j.1551-8833.1968.tb03660.x.
[5] Jennings PC. Engineering features of the san Fernando earthquake of february 9, 1971. Pasadena, CA: California Institute of Technology; 1971.
[6] CH2MHILL. Buried reservoir seismic program. Washington: Seattle; 2015. Report CH2MHILL.
[7] Hushmand A, Dashti S, Davis C, Hushmand B, Zhang M, Ghayoomi M, McCartney J, Lee Y, Hu J. Seismic performance of underground reservoir structures: Insight from centrifuge modeling on the influence of structure stiffness. J Geotech Geoenviron Eng 2016;142(7):04016020. https://doi.org/10.1061/(ASCE)GT.1943-5606.0001477.
[8] Hushmand A, Dashti S, Davis C, McCartney J, Hushmand B. A centrifuge study of the influence of site response, relative stiffness, and kinematic constraints on the seismic performance of buried reservoir structures. Soil Dynam. Earthquake Eng 2016;88:427–38. https://doi.org/10.1016/j.soildyn.2016.06.011.
[9] Harounian A, Davis CA, Lew M, Hudson MB. Going beyond code-based design: use of advanced numerical modeling to support design of Los Angeles's Headworks reservoir. In: *Proc. Geo-congress 2014*, Atlanta, Georgia; 2014. https://doi.org/10.1061/9780784413272.296.
[10] Hudson MB, Davis CA, Lew M, Harounian A. Seismic resilience design for a concrete box reservoir. In: Proc. 6th China-Japan-US trilateral symposium on lifeline earthquake engineering; 2014. https://doi.org/10.1061/9780784413234.018.
[11] Deng Y, Dashti S, Hushmand A, Davis C, Hushmand B. Seismic response of underground reservoir structures in sand: evaluation of Class-C and C1 numerical simulations using centrifuge experiments. Soil Dynam. Earthquake Eng 2016;85: 202–16. https://doi.org/10.1016/j.soildyn.2016.04.003.
[12] Zhang W, Seylabi EE, Taciroglu E. Effects of soil stratigraphy on dynamic soil-structure interaction behavior of large underground structures. In: Proc. 3rd international conference on performance-based design in earthquake geotechnical engineering (PBDIII); 2017. Vancouver, Canada.
[13] LSTC. LS-Dyna keyword user's manual. Livermore Software Technology Corporation; 2020.
[14] AlKhatib K, Hashash YMA, Ziotopoulou K, Heins J. Centrifuge and numerical modeling of the seismic response of buried water supply reservoirs. J Geotech Geoenviron Eng 2024;150(3):04023141. https://doi.org/10.1061/JGGEFK.GTENG-11758.
[15] Morales B. Centrifuge modeling of hydrodynamic loads in water storage tanks. Davis: University of California; 2020. M.S. thesis.
[16] Morales B, Ziotopoulou K, Hashash YMA, AlKhatib K. Large centrifuge experiments of hydrodynamic loading in water tanks. DesignSafe -CI PRJ-3192 2024. https://doi.org/10.17603/ds2-5spt-gv81.
[17] AlKhatib K, Hashash YMA, Ziotopoulou K, Morales B. Hydrodynamic pressures on rigid walls subjected to cyclic and seismic ground motions. Earthq Engng Struct Dyn 2023;53(1):279–302. https://doi.org/10.1002/eqe.4020.
[18] Heins JV, Ziotopoulou K, Hashash YMA, AlKhatib K. JVH01 and JVH02: centrifuge test of buried water reservoir – rotated reservoir orientation. In: Centrifuge modeling of buried water reservoirs. DesignSafe-CI PRJ-3181; 2024. https://doi.org/10.17603/ds2-ptc4-nx84.
[19] Kutter BL. Recent advances in centrifuge modeling of seismic shaking. In: Proc. Third international conference on recent advances in geotechnical earthquake engineering and soil dynamics; 1995. p. 927–42. St. Louis, Missouri.
[20] Boulanger RW. Effect of model container on dynamic shear stresses in a centrifuge model. 8th international conference on earthquake geotechnical engineering, osaka, Japan, may 7-10. 2024.
[21] ASCE/SEI 7-22. Minimum Design Loads and Associated Criteria for Buildings and Other Structures. Reston, VA: American Society of Civil Engineers; 2022.
[22] Bolton M. The strength and dilatancy of sands. Geotechnique 1986;36(1):65–78. https://doi.org/10.1680/geot.1986.36.1.65.
[23] Darendeli MB. Development of a new family of normalized modulus reduction and material damping curves. Univ. of Texas at Austin; 2001. Ph.D. thesis.
[24] Groholski DR, Hashash YM, Kim B, Musgrove M, Harmon J, Stewart JP. Simplified model for small-strain nonlinearity and strength in 1D seismic site response analysis. J Geotech Geoenviron Eng 2016;142(9):04016042. https://doi.org/10.1061/(ASCE)GT.1943-5606.0001496.
[25] Numanoglu OA, Hashash YMA, Olson SM, Cerna-Diaz A, Rutherford CJ, Bhaumik L, Centella R DM, Weaver T. A simplified three-dimensional constitutive model for seismic modeling of dense sands. Soil Dynam Earthq Eng 2023;167: 107794. https://doi.org/10.1016/j.soildyn.2023.107794.
[26] Kwak D, Ahdi S, Wang P, Zimmaro P, Brandenberg S, Stewart J. Web portal for shear wave velocity and HVSR databases in support of site response research and applications. UCLA Geotechnical Engineering Group; 2021. https://doi.org/10.21222/C27H0V.
[27] Mander JB, Priestley MJ, Park R. Theoretical stress-strain model for confined concrete. Journal of structural engineering 1988;114(8):1804–26. https://doi.org/10.1061/(ASCE)0733944451988114:81804.
[28] AlKhatib K. Seismic fluid-structure-soil interaction of buried water reservoirs. Ph. D. thesis. University of Illinois Urbana-Champaign; 2023.
[29] Chakrabarti SK. Wave forces on multiple vertical cylinders. J. Waterway, Port, Coastal Ocean Div. 1978;104(WW2):147–61. https://doi.org/10.1061/JWPCDX.0000084.
[30] ACI 318-19. Building code requirements for structural concrete (ACI 318-19) and commentary, AlKhatib, K. 2023. "Seismic fluid-structure-soil interaction of buried water reservoirs" Ph.D. thesis. Urbana-Champaign: University of Illinois; 2019.